Journal of Materials Chemistry A

Tetragonal C24: A Topological Nodal-surface Semimetal with Potential as an Anode Material for Sodium Ion Batteries

Journal:	*Journal of Materials Chemistry A*
Manuscript ID	TA-ART-11-2018-011276.R2
Article Type:	Paper
Date Submitted by the Author:	09-Feb-2019
Complete List of Authors:	Qie, Yu; Peking University, college of engineer Liu, Junyi; Peking University, Wang, Shuo; Peking University, Materials Science and Engineering Sun, Qiang; Peking University, Jena, Purusottam ; Virginia Commonwealth University, Physics Department

SCHOLARONE™
Manuscripts

Tetragonal C_{24}: A Topological Nodal-surface Semimetal with Potential as an Anode Material for Sodium Ion Batteries

Yu Qie,[a] Junyi Liu,[a] Shuo Wang,[a] Qiang Sun,[a,b,c,*] and Puru Jena[c]

[a] Department of Materials Science and Engineering, Peking University, Beijing 100871, China

[b] Center for Applied Physics and Technology, Peking University, Beijing 100871, China

[c] Department of Physics, Virginia Commonwealth University, Richmond, VA 23284, USA

*Email - sunqiang@pku.edu.cn

Abstract

Na-ion batteries, as an alternative to Li-ion batteries, have gained increasing attention due to the abundance of sodium and its low cost. In the present work, we propose a 3D porous carbon material by inserting hexagonal carbon rings into sp^3 C-C bonds in a previously established 3D-(4,4) lattice, termed as tC_{24}. *Ab initio* calculations uncover that not only tC_{24} is thermally, dynamically and mechanically stable, but also exhibits a unique electronic band structure with two topological nodal surfaces traversing through the whole Brillouin zone. More importantly, tC_{24} is the *first* all carbon topological *nodal-surface semimetal for Na-ion batteries*, exhibiting a high theoretical capacity of 232.65 $mAhg^{-1}$, low diffusion energy barrier for Na ions, appropriate average voltage of 0.54 V and negligible volume change (~0.94%) during charging/discharging operation. These properties empower tC_{24} with a potentially long cycle life when used as an anode material for Na-ion batteries.

1. Introduction

Na-ion batteries (NIBs) have received a great deal of interest in recent years due to the high abundance, low cost and environment-friendly nature of sodium [1, 2], making them an attractive alternative to Li-ion batteries (LIBs) for large-scale applications [3, 4]. Because of its larger ionic radius (1.02 Å compared to 0.76 Å for Li) and different electrochemical properties, Na significantly affects the performance of the anode materials for NIBs, and strongly influences their kinetic and thermodynamic properties. For example, the widely used graphite anode for LIBs is not suitable for NIBs due to the poor specific capacity (35 $mAhg^{-1}$) [5, 6]. Thus, it is highly desirable to develop non-graphitic carbon materials for NIBs [5, 7, 8]. However, currently synthesized porous carbon materials are amorphous, making the disordered pores and structural defects unfavorable for Na-ion transport and electronic conductivity [9-11]. Therefore, carbon allotropes with regularly distributed pores and intrinsic metallicity are highly desirable. The recently proposed 3D topological semimetal (TSM) carbon materials satisfy the above criteria and are supposed to be promising anode candidates for NIBs because of the good electronic conductivity as well as the regularly porous structure, which provides sufficient space for the intercalation/de-intercalation of Na ions, guaranteeing reasonable capacity, moderate volumetric change and acceptable ionic conductivity [12-16]. Besides, theoretical studies have shown that 3D TSM carbon materials could exhibit excellent performance when used as anodes for LIBs [17, 18].

Motivated by the above works, we have explored the potential of carbon TSMs with suitable pore size to accommodate Na ions and to lead to the development of rechargeable long-life NIBs. In this paper, we report a network of carbon allotrope tC_{24} that has tetragonal symmetry and contains 24 atoms in a unit cell. This is constructed by inserting hexagonal carbon rings into sp^3 C-C bonds in a previously reported tC_8 with 3D-(4,4) lattice [19]. Electronic band structure calculation reveals that tC_{24} is a topological nodal-surface semimetal, which possesses two mirror-symmetric nodal surfaces, traversing through the whole Brillouin zone (BZ). Calculations also show surface flat bands around the Fermi level, bounded by the projection of the bulk nodal surface. Furthermore, we explore the potential of tC_{24} as an anode material for NIBs, in recognition of its regularly distributed channels for ion transport and intrinsic conductivity for electron transport. This anode material possesses a usable theoretical capacity of 232.65 $mAhg^{-1}$, an average voltage of 0.54 V, low energy barriers for Na ions to diffuse, and nearly zero volume change during charging/discharging operation, ensuring a potentially long cycle life.

2. Computational Methods

All calculations are carried out using Vienna *ab initio* Simulation Package code (VASP) [20] within the framework of density functional theory. The projector augmented wave (PAW) [21] potential is adopted to consider the electron-ion interactions. The electron-electron interaction is treated using the generalized gradient approximation (GGA) to the exchange-correlation functional [22] given by Perdew-Burke-Ernzerhof (PBE). The Heyd-Scuseria-Ernzerhof (HSE06) [23, 24] hybrid functional is also used for improving the accuracy of electronic structure calculations. The plane-wave cutoff energy for wave function is set to 600 eV. van der Waals (vdW) interactions are taken into account by using a semi-empirical correction of Grimme's D2 scheme [25]. The structure optimizations are carried out using the conjugated gradient method with the convergence thresholds of 10^{-6} eV and 10^{-3} eV/Å for total energy and force component, respectively. The first Brillouin zone is sampled by a k-point mesh with a grid density of $2\pi\times0.02$ $Å^{-1}$ using the Monkhorst-Pack scheme [26]. *Ab initio* molecular dynamics (AIMD) simulation at room temperature is performed using the canonical ensemble (NVT) with the Nosé-Hoover heat bath scheme [27] in a 1×1×5 supercell to examine thermal stability. Phonon spectrum is calculated using finite displacement method as implemented in the Phonopy code [28]. The band symmetric representations and slice band structures are calculated with the help of Quantum ESPRESSO [29] and Wannier Tools package [30], respectively. The diffusion energy barriers for Na ions and the charge population analysis are calculated by using the climbing-image nudged elastic band (CI-NEB) method [31, 32] and Bader charge [33].

The stable intermediate configurations at various Na concentrations are accurately determined by using cluster expansion (CE) method, based on which the Na_x-tC_{24} system is treated as an alloy. We represent each possible Na cation at site i with an occupation variable σ_i, which takes the value 1 if cation resides at that site and −1 if a vacancy is at that site. The configuration-dependent Hamiltonian is mapped onto a generalized Ising Hamiltonian,

$$E(\sigma) = J_0 + \sum_i J_i \sigma_i + \sum_{j<i} J_{ij} \sigma_i \sigma_j + \sum_{k<j<i} J_i \sigma_i \sigma_j \sigma_k + ... = J_0 + \sum_\alpha J_\alpha \varphi_\alpha , \qquad (1)$$

where the subscripts i, j, and k range over all occupation sites, φ_α is the product of occupation variables σ_i, σ_j … σ_k that forms a cluster configuration α, which can be a single point, a pair of clusters or a triplet cluster, etc. J_α is the corresponding effective cluster interactions (ECI), which is obtained by fitting these to the first-principles calculated energies of selected configurations. The quality of the fitted CE is measured by the cross-validation (CV) score, and the fitting process is performed by using Alloy Theoretic Automated Toolkit (ATAT) code [34]. When the CE fittings reach a high accuracy, namely, a reasonably low CV score, it is able to calculate the configurational energy and give a reliable prediction for the lowest-energy configurations.

3. Results and discussion

3.1 Structure and stability of tC_{24}

The structure of tC_{24} is constructed by inserting hexagonal carbon rings into the sp^3 C-C bonds in a previously reported carbon structure tC_8 [19], similar to bct-C_{40}, which can also be constructed by inserting hexagonal carbon rings into C-C bonds in the bct-C4 lattice [16]. The unit cell contains 24 atoms and its space group is D_{4h}-1 (No. 123, P4/mmm). The optimized lattice parameters are a=b=11.304 Å and c=2.474 Å with the carbon atoms occupying four inequivalent Wyckoff positions of 8q (0.2811, 0.8959, 0.5) (gray), 8p (0.2393, 0.8515, 0.0) (green), 4m (0.0, 0.3676, 0.5) (black) and 4l (0.0, 0.5591, 0.0) (red), denoted by C1, C2, C3 and C4, respectively (see Figure 1). There are five distinct bond lengths: two bonds of 1.417 (C1-C2) and 1.450 Å (C2-C2) are in the inserted hexagonal carbon rings and close to the bond length of 1.420 Å in graphite; two longer bonds of 1.530 (C1-C3) and 1.489 Å (C3-C4) are associated with C1-C3 and C3-C4 sp^3 bonds, respectively. Meanwhile, one shorter bond of 1.335 Å with ethene-type C4=C4 double bond is formed as in all-sp^2 carbene. There are also five distinct bond angles: two bond angles of C1-C2-C2=119.13°, C2-C1-C2=121.71° are in the inserted hexagonal carbon rings and three bond angles of C4-C3-C4=112.33°, C1-C3-C4=110.84° and C1-C3-C1=95.51° are on average close to the 109.5° angle in diamond. Furthermore, tC_{24} has two types of 1D nanotube channels along the ***c*** direction: one is an octagonal channel with a pore size of 9.78 Å and another is a quadrangle channel with a smaller pore size of 5.88 Å, leading to a porous structure with a mass density of 1.52 g/cm^3. This density is much less than those of the diamond (3.55 g/cm^3), graphite (2.24 g/cm^3) and tC_8 (2.40 g/cm^3) [19]. The nanopores could accommodate other species such as atoms or molecules for further functionalization. To get a better understanding of the bonding nature, the extended view is also illustrated in Figure 1(b) with a 3×3×5 supercell. It should be mentioned that the calculated lattice parameters and bond lengths with and without vdW corrections are almost the same (Table S1), suggesting that the effect of vdW corrections on the structural parameters of tC_{24} is subtle and negligible. Therefore, the following calculations of the thermodynamic, dynamical and mechanical properties of tC_{24} are carried out using the standard PBE exchange-correlation functional, without vdW corrections.

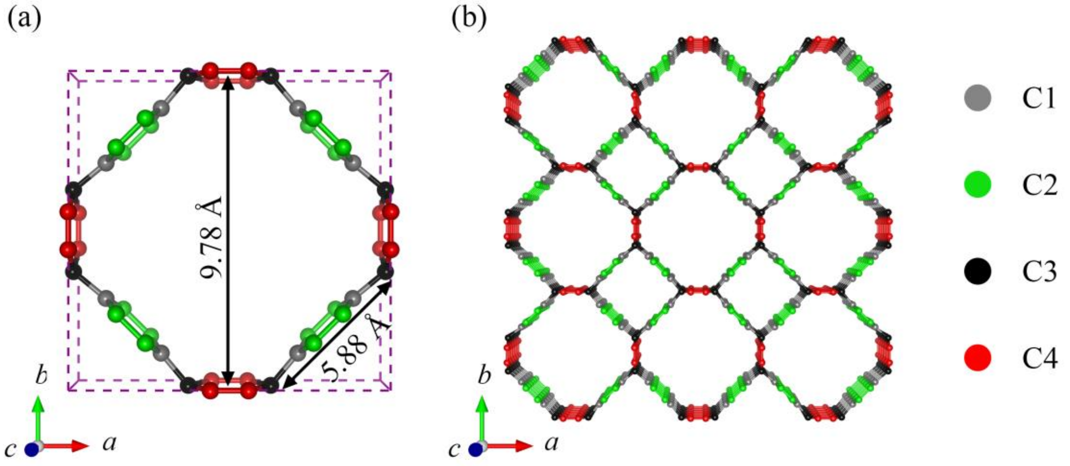

Figure 1. (a) The 24-atom unit cell of tC_{24}. (b) The extended view of tC_{24} carbon with a 3×3×5 supercell.

To investigate the stability of tC_{24}, we first calculate its total energy per atom as a function of volume and compared these with other carbon phases, including graphite, diamond, and recently reported structures, such as IGN-C_6 [12] , bct-C_{40} [16], bct-C_{16} [15], T-carbon[35] and tC_8 [19]. The results are plotted in Figure S1. In spite of the fact that tC_{24} is 0.218 eV/atom and 0.085 eV/atom higher in energy than graphite and diamond, respectively, it is more stable than bct-C_{16}, IGN-C_6, T-carbon and tC_8. Next, the phonon band structure of tC_{24} is calculated to study its dynamical stability. The results are presented in Figure S2(a); the phonon spectrum shows no imaginary modes in the entire BZ, confirming the dynamic stability of tC_{24}. Furthermore, AIMD simulation is carried out by constructing a 1×1×5 supercell containing 120 atoms to examine the thermal stability tC_{24}. As shown in Figure S2(b), after being heated at temperature of 300 K for 5 picoseconds (ps), the structure remains nearly intact without apparent distortion, and the total energy only fluctuates around a constant value, suggesting that tC_{24} is thermally stable at room temperature. Finally, to verify the mechanical stability of tC_{24}, we calculated the independent elastic constants under small lattice distortion. The calculated results are listed in Table S2, which satisfy the Born-Huang criteria for tetragonal lattice [36]: $C_{11} > |C_{12}|,\ 2C_{13}^2 < C_{33}(C_{11}+C_{22}),\ C_{44} > 0, C_{66} > 0$, confirming that the tC_{24} structure is mechanically stable.

3.2 Electronic properties

We next discuss the electronic properties of tC_{24}. Different form tC_8, which is a semiconductor with a band gap of 0.93 eV [19](see Figure S4), tC_{24} is a semimetal. The band structure, calculated by using the DFT-GGA/PBE functional, is shown by blue line in Figure 2(a). Note that the valence and conduction bands of tC_{24} exhibit linear dispersion near the Fermi level and cross along the A-M, Γ-Z and X-R high symmetry directions, which suggests that tC_{24} is semimetallic. To validate the results obtained by the PBE functional, we have recalculated the band structure of tC_{24} by using HSE06 hybrid functional. The results are shown in red lines in Figure 2(a). Note that the semimetallic feature of tC_{24} is preserved at the HSE06 level. The effect of the vdW interaction on the band structure is further checked and found to be neglected as the band structure remains almost unchanged when the vdW interaction is included (see Figure. S5 for details). On further analysis, both the conduction band (CB) and valence band (VB) along the high symmetry A-M, Γ-Z and X-R lines belong to the same point group (C_{4v}), but differ in their symmetric representations. As shown in the insert in Figure 2(a), the VB and CB along the high symmetry path A-M belong to two different irreducible representations A_1 and A_2, respectively. Along with the intersection of CB and VB, their energy ordering exchanges, leading to the so-called band inversion, which is one of the key ingredients in topological semimetals, confirming our conclusion that tC_{24} is a topological semimetal. Similarly, the band crossings along the high symmetry lines Γ-Z and X-R have the same feature. In addition, as shown in Figure 2(b), the partial density of states (PDOS), projected to non-equivalent atomic orbitals, indicates that the bands near the Fermi level mainly originate from the $\boldsymbol{p_x}$ and $\boldsymbol{p_y}$ orbitals of the inserted hexagonal carbon ring atoms (C1 and C2).

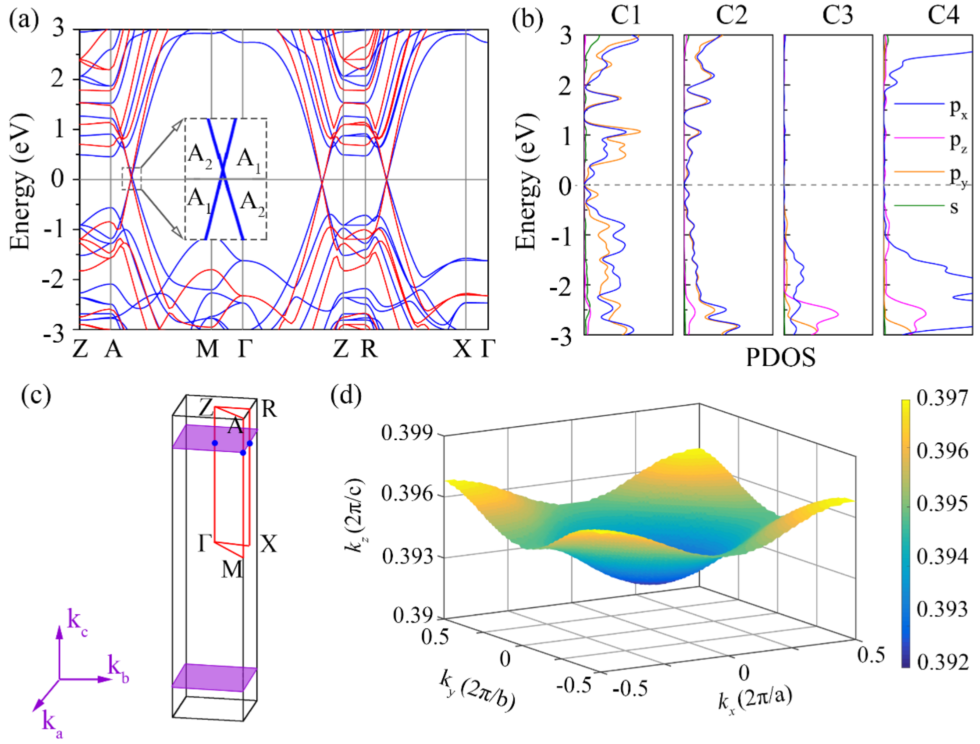

Figure 2. (a) Electronic band structures of tC_{24} (the red/blue lines represent the HSE06/PBE results). (b) Partial density of states projected to nonequivalent atomic orbitals. (c) The bulk BZ with high symmetry points, two symmetric nodal surfaces marked in light purple color, and the three blue dots are the Dirac points along the A-M, Γ-Z and R-X paths in the band structure in (a). (d) The enlarged view of the above nodal surface.

Further analysis of the band structure of tC_{24} in the whole BZ indicates that the band crossing points of CB and VB form two quasi-plane nodal surfaces spanning the entire BZ, which are time-reversal and inversion images of each other, as schematically shown in Figure 2(c). Zooming into the above nodal surface, we can see that the surface has a basin-like shape and the band crossing along line Γ-Z is closer to Γ, while the crossing along line X-R is nearer to R, as shown in Figure 2(d). It is known that the spin-orbit coupling (SOC) may open up a gap at the band crossing points. For the case of tC_{24}, a very small band gap of 1.3 meV along Γ-Z, X-R and A-M directions is estimated when the SOC is considered (see Figure S6), making tC_{24} a 3D weak topological insulator with a Z_2 index of (0:110). Thus, the SOC in tC_{24} can be neglected and is not expected to alter the semimetallic feature at room temperature.

It is known that one of the exotic features of topological materials is the robust edge states or surface states, which is approximately dispersion-less in a subset of the 2D edge Brillouin zone, given by the projection of the nodal surfaces or line nodes onto the plane of the edge [37]. Thus, flat surface states would exist whether the dangling bonds are saturated with hydrogen atoms or not. Here, leaving the surface dangling bonds alone and constructing a 10-layer-thick slab along the $[100]$ direction of the primitive cell, we calculate the surface band by using *Wannier tools* [30]. The results for the semimetallic tC_{24} are presented in Figure 3(b), which show that there indeed exists a nearly flat band around the Fermi level.

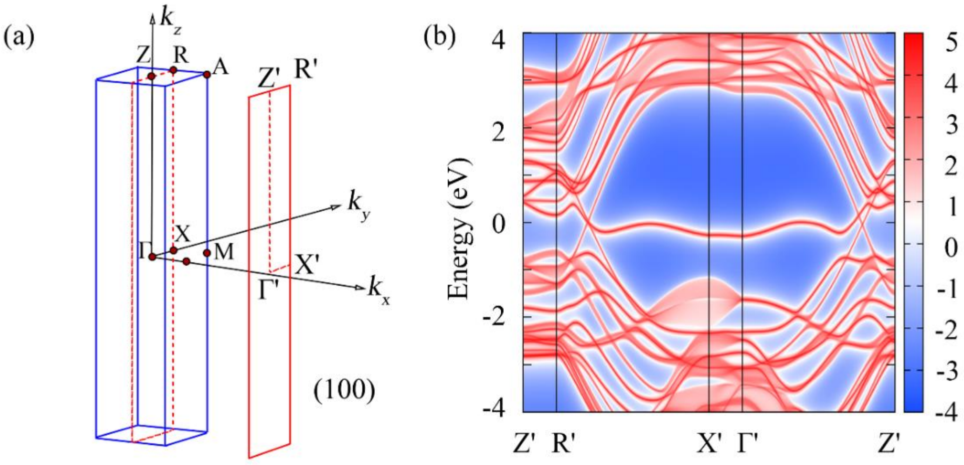

Figure 3. (a) Bulk and (100)-surface BZ (indicated by the red rectangle) of tC_{24}, as well as the high-symmetry k points. (b) Surface states analysis of the tC_{24} (100) surface.

3.3 Potential Application of tC_{24} as an Anode Material for Na-Ion Batteries

Considering its regularly distributed channels and intrinsic metallicity, we expect that tC_{24} could be a promising carbon-based anode material for NIBs. To examine this possibility, we systematically investigated the binding and diffusion behavior of Na as well as the theoretical capacity, open-circuit voltage (OCV), and volume change during the ion intercalation/de-intercalation process.

First we calculate the binding energy (E_b) of a single Na atom using a 1×1×5 supercell of tC_{24} to estimate the binding strength according to the following equation:

$$E_b = (E_{Na_x - tC_{24}} - E_{tC_{24}} - x\mu_{Na}) / x \,, \qquad (2)$$

where $E_{Na_x - tC_{24}}$ and $E_{tC_{24}}$ are the total energies of Na-inserted and pristine tC_{24} structure, respectively, μ_{Na} is the chemical potential of the reference metallic Na; negative E_b indicates an exothermic reaction. The effect of the vdW interaction on the geometry of the Na adsorbed tC_{24}, and on the kinetic of Na atoms in the structure of tC_{24} is taken into account by using semiempirical long-range dispersion correction (the PBE-D2 functional). As seen from Figure 4, according to the geometrical symmetry of tC_{24}, five possible initial adsorption sites are considered; three hollow sites of octagonal channel

(H1~H3) and two hollow sites of the quadrangle channel (H5, H6). After structure optimizations, H1 and H4 led to H3 and H5, respectively. H2, H3, and H5 sites are found to be stable adsorption sites with binding energies of -0.47, -0.89 and -1.09 eV, respectively, suggesting that the H5 site (the hollow site of quadrangle channel) is energetically the most favorable binding site for the Na atom. Furthermore, Bader charge analysis shows that almost all valence electrons of Na atoms are transferred to the neighboring C atoms when adsorbed onto the H2, H3 and H5 sites (0.90, 0.87 and 0.89 e^-, respectively). This leads to a strong ionic interaction between the Na cation and tC_{24}. The resulting Coulomb repulsion between the adsorbed Na ions prevent them from clustering. Besides, in accordance with the discussion in Supplemental Material, the maximum capacity of tC_{24} corresponds to the Na concentration at which the slope of the formation energy curve becomes positive. As shown in Figure S6, the stoichiometric formula of maximum Na-intercalated tC_{24} is determined to be Na_5C_{48}. The corresponding geometry is displayed in Figure S8, where only H3 and H5 sites are occupied due to the space constraint. The resulting theoretical specific capacity is 232.65 mAh/g, which is larger than those of MoS_2 (146 mAh/g) [38], open-cage allotrope Si_{24} (159.5 mAh/g) [39], ISN (159.5 mAh/g) [40], and comparable to that of hard carbon (250 mAh/g) [41].

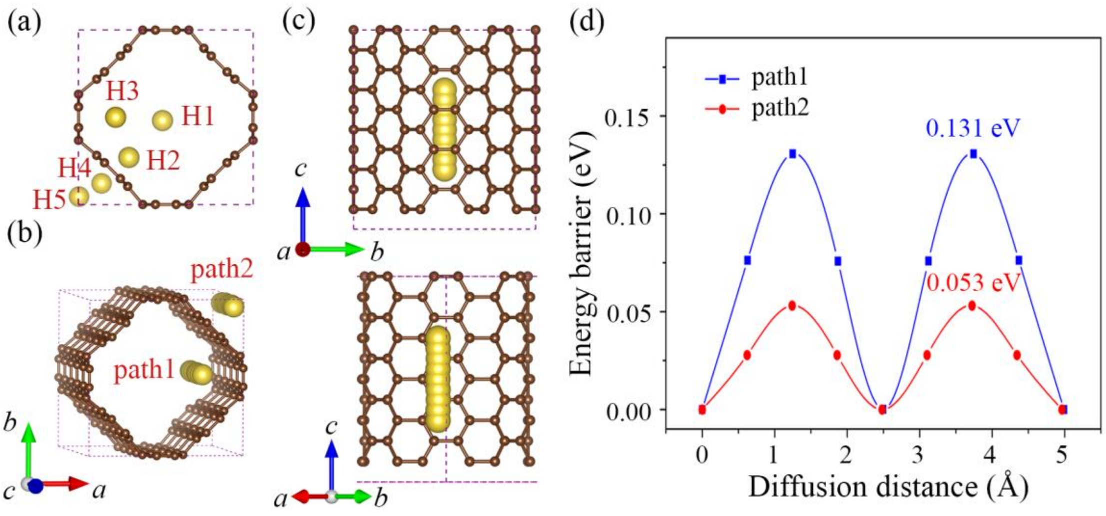

Figure 4. (a) Top view of the considered adsorption sites. (b) The considered Na-ion migration paths and (c) the comparison between diffusion path1 (up) and path2 (down).

(d) Diffusion energy barrier profile of Na diffusion in tC_{24}. The yellow and brown spheres represent sodium and carbon atoms, respectively.

The potential of tC_{24} as an anode material for NIBs also depends on the mobility of the Na ions. Therefore, we have studied the diffusion behavior of dilute Na cations in tC_{24} by using CI-NEB method. At the beginning, Na atom is introduced to the framework of tC24. Once adsorbed, almost all valence electrons of Na atom are transferred to the neighboring C atoms (around 0.9 e- by Bader charge analysis), leading to Na ions migrating along the diffusion path. Here, we only consider diffusion paths along the ***c*** direction because when Na atom interpenetrates through the carbon hexagon ring, the energy barrier is nearly 20 eV (see Figure S9), blocking it from migration along the ***ab*** plane. Considering the structural symmetry and the occupied Na sites in the fully-intercalated tC_{24}, we select two representative diffusion pathways, as presented in Figure 4(b). Path1 and 2 are along the ***c*** direction of the octagonal hollow channel and quadrangle hollow channel connecting adjacent H3 and H5 sites, respectively. The corresponding diffusion energy profiles are shown in Figure 4(d). Note that the diffusion barriers of the two paths are 0.131 eV (path1) and 0.053 eV (path2), respectively, showing one-dimensional diffusion paths along the channels, similar to the diffusion behavior along the pores of nanotube materials [40, 42, 43]. It is interesting to note that the diffusion barrier along octagonal channel with a larger pore size (path1) is greater than that along the quadrangle channel (path2). To understand the reason behind, we compare the two different local migration environments as shown in Figure 4(c). Along the octagonal channel (path1), Na-ion migrates across C-C bonds where the electrons are localized, which leads to a dramatic change in the energy landscape, resulting in the higher diffusion barrier along the octagonal channel. On the other hand, along quadrangle channel (path2), Na-ion diffuses along the zigzag carbon chain where the electrons are delocalized, leading to a flatter energy landscape and a smaller energy barrier. The diffusion barriers of tC_{24} are smaller than that of black phosphorus (0.18~0.76 eV) [44], MoS_2 (0.28 eV) [38], and even less than those of several

2D materials, such as silicene (0.16 eV) [45], BC_3 (0.16~0.22 eV) [46] and TiC_3 monolayer (0.18~0.31 eV) [47], indicating high Na-ion mobility and good charge/discharge rate when tC_{24} is used as an anode for NIBs.

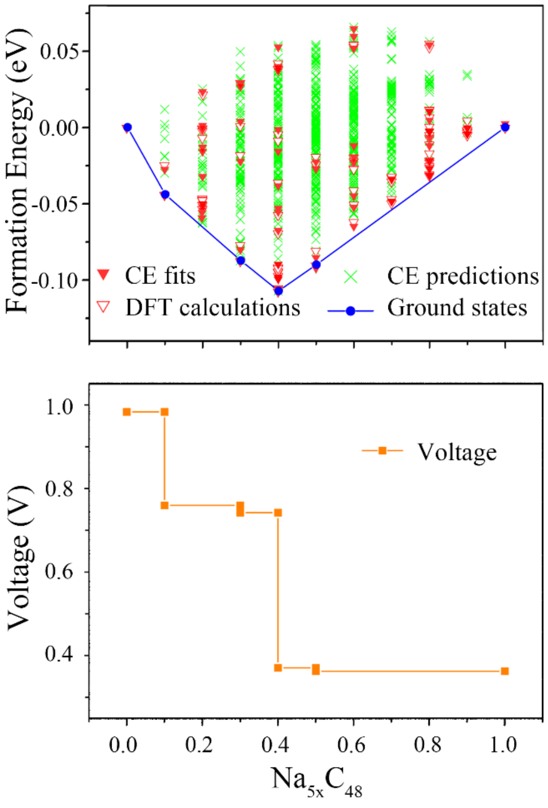

Figure 5. (a) Formation energies predicted by CE method for various Na concentrations for four stable intermediate phases, (b) the corresponding voltage profile.

The open-circuit voltage profile is another key factor to assess the performance of anode materials. To test electrode performance in general, the charge/discharge process of tC_{24} needs to comply with the following half-cell reaction *versus* Na/Na^+:

$$(x_2-x_1)Na^+ + (x_2-x_1)e^- + Na_{x_1}\text{-}tC_{24} \leftrightarrow Na_{x_2}\text{-}tC_{24}. \qquad (3)$$

When the effects of volume, pressure and entropy are neglected, the average voltage of Na_x-tC_{24} in the concentration range of $x_1 < x < x_2$ can be estimated by using the following formula:

$$V \approx \frac{E_{Na_{x_1}-tC_{24}} - E_{Na_{x_2}-tC_{24}} + (x_2-x_1)\mu_{Na}}{(x_2-x_1)}, \qquad (4)$$

where $E_{Na_{x_1}-tC_{24}}$, $E_{Na_{x_2}-tC_{24}}$ and μ_{Na} are the total energy of Na_{x1}-tC_{24}, Na_{x2}-tC_{24}, and per Na atom in bulk phase, respectively. Therefore, it is necessary to accurately determine the stable intermediate phases in order to calculate the step voltage. To this end, CE method is applied and the Hamiltonian of Na_x-tC_{24} is constructed by fitting to the first principles calculated energies of 81 configurations with varying Na concentrations. The CV score of the CE fitting is 18 meV, small enough to guarantee the accuracy of CE Hamiltonian prediction of intermediate configurations of Na_x-tC_{24}. As the results presented in Figure 5(a) show, there are four stable intermediate structures with corresponding Na concentrations of 0.1, 0.3, 0.4 and 0.5. The corresponding geometries are presented in Figure S10 (See Supplemental Material). Next, we calculate the step OCV profile based on Eq. (4). The corresponding result is displayed in Figure 5(b), where we can see that there are three prominent voltage regions: $0 < x < 0.1$, the large voltage plateau value of 0.98 eV could be ascribed to the strong binding of Na with tC_{24}; $0.1 < x < 0.4$, a region with a plateau value of around 0.75 eV; $0.4 < x < 1.0$, there is a dramatic drop from 0.74 to 0.37 V at the sodium concentration of 0.4, which is due to the increasing repulsive interaction between the Na ions. Besides, the voltage remains positive throughout the whole process, suggesting that half-cell reaction can go on spontaneously to reach the final phase (Na_5C_{48}). Thus, tC_{24} performs as an anode with a fully reversible capacity of 232.65 mAh/g. By numerically averaging the voltage profile in the whole region, the corresponding average voltage is 0.54 V, smaller than that of $Li_4Ti_5O_{12}$ (0.91 V) [48] and MoS_2 (1.25 V) [38], and larger than that of hard carbon (0.01 eV) [49] and TiC_3 (0.18 V) [47]. The average voltage of tC_{24} would not only prevent the formation of dendrites but also the formation of SEI. These will enhance battery safety as well as improve the cycling of the battery, without sacrificing the energy density too much. These are important considerations for practical applications [4]. In addition, the DOS of these Na_x-tC_{24} structures (See Figure S11) suggests that the studied tC_{24} anode will maintain the metallic feature with a good electronic conductivity before and after Na atoms are intercalated. Moreover, compared with the pristine tC_{24} structure, the volume changes of the intermediate stable Na-inserted structures are less than 0.94%, which is significantly smaller than that of alloy anode materials [44, 50], and even smaller than ISN (2.8%) [40], indicating that tC_{24} can accommodate Na ions reversibly with an excellent cycling stability.

4. Conclusions

In summary, using first-principles calculations, combined with cluster expansion method, we have proposed a stable 3D carbon allotrope tC_{24} constructed by inserting hexagonal carbon rings into the sp^3 C-C bonds in a previous reported tC_8 lattice. Its structural stabilities are verified by phonon mode analysis, AIMD simulation, and Born-Huang criteria. Total energy calculations show that tC_{24} is more stable than bct-C_{16}, IGN-C_6, T-carbon and tC_8. Electronic structure calculations demonstrate that the tC_{24} possesses two nontrivial topological nodal surfaces in the BZ, protected by time reversal and inversion symmetry. Moreover, there exists a flat band, localized around the Fermi level when the bulk nodal surface is projected onto a surface. We show that tC_{24} is a promising anode material for Na-ion batteries with a high reversible capacity of 232.65 mAh/g, low diffusion energy barriers (0.053~0.131 eV), relatively high average voltage of 0.54 V, intrinsic metallic property and also negligible volume change (0.94%). Our study reveals the great potential of 3D carbon TSMs with intrinsic metallicity and ordered pores for anode materials in NIBs. We hope that these findings will motivate further theoretical and experimental efforts to develop new 3D carbon TSMs for high-performance NIB anode materials. In addition, Zhang et al. reported a method to synthesis a previously predicted carbon allotrope, T-carbon with a quite small equilibrium density (1.50 g/cm^3) by picosecond pulsed-laser irradiation of a multi-walled carbon nanotube suspension suspension in methanol [51]. Considering the lower energy of tC_{24}, we can expect that tC_{24} could also be realized in the future.

ACKNOWLEDGMENTS

This work is partially supported by grants from the National Key Research and Development Program of China (2016YFB0100200), and from the National Natural Science Foundation of China (21573008 and 21773003). P. J. acknowledge support by the U.S DOE, Office of Basic Energy Sciences, Division of Material Sciences and

Engineering under Award No. DE-FG02-96ER45579. The calculations are supported by High-performance Computing Platform of Peking University.

Reference

1. B. L. Ellis and L. F. Nazar, *Curr. Opin. Obstet. Gyn.*, 2012, **16**, 168-177.
2. S. W. Kim, D. H. Seo, X. Ma, G. Ceder and K. Kang, *Adv. Energy Mater.*, 2012, **2**, 710-721.
3. S. Y. Hong, Y. Kim, Y. Park, A. Choi, N.-S. Choi and K. T. Lee, *Energy Environ. Sci.*, 2013, **6**, 2067-2081.
4. K. Chayambuka, G. Mulder, D. L. Danilov and P. H. L. Notten, *Adv. Energy Mater.*, 2018, **8**, 1800079.
5. D. A. S. a. J. R. Dahn, *J. Electrochem. Soc.*, 2001, **148**, A803-A811.
6. P. Ge and M. Fouletier, *Solid State Ionics*, 1988, **28-30**, 1172-1175.
7. R. Alcántara, P. Lavela, G. F. Ortiz and J. L. Tirado, *Electrochem. Solid State Lett.*, 2005, **8**, A222-A225.
8. J. Xu, M. Wang, P. Wickramaratne Nilantha, M. Jaroniec, S. Dou and L. Dai, *Adv. Mater.*, 2015, **27**, 2042-2048.
9. H. Hou, C. E. Banks, M. Jing, Y. Zhang and X. Ji, *Adv. Mater.*, 2015, **27**, 7861-7866.
10. J. Hou, C. Cao, F. Idrees and X. Ma, *ACS Nano*, 2015, **9**, 2556-2564.
11. X. Deng, B. Zhao, Y. Sha, Y. Zhu, X. Xu and Z. Shao, *ChemElectroChem*, 2016, **3**, 698-703.
12. Y. Chen, Y. Xie, S. A. Yang, H. Pan, F. Zhang, M. L. Cohen and S. Zhang, *Nano Lett.*, 2015, **15**, 6974-6978.
13. H. Weng, Y. Liang, Q. Xu, R. Yu, Z. Fang, X. Dai and Y. Kawazoe, *Phys. Rev. B*, 2015, **92**.
14. J. T. Wang, H. Weng, S. Nie, Z. Fang, Y. Kawazoe and C. Chen, *Phys. Rev. Lett.*, 2016, **116**, 195501.
15. Y. Cheng, X. Feng, X. Cao, B. Wen, Q. Wang, Y. Kawazoe and P. Jena, *Small*, 2017, **13**.
16. J. T. Wang, S. Nie, H. Weng, Y. Kawazoe and C. Chen, *Phys. Rev. Lett.*, 2018, **120**, 026402.
17. J. Liu, S. Wang and Q. Sun, *Proc. Natl. Acad. Sci.*, 2017, **114**, 651.
18. J. Liu, S. Wang, Y. Qie, C. Zhang and Q. Sun, *Physical Review Materials*, 2018, **2**, 025403.
19. Z. Zhao, B. Xu, L.-M. Wang, X.-F. Zhou, J. He, Z. Liu, H.-T. Wang and Y. Tian, *ACS Nano*, 2011, **5**, 7226-7234.
20. G. Kresse and J. Furthmüller, *Phys. Rev. B*, 1996, **54**, 11169-11186.
21. P. E. Blöchl, *Phys. Rev. B*, 1994, **50**, 17953-17979.
22. J. P. Perdew, K. Burke and M. Ernzerhof, *Phys. Rev. Lett.*, 1996, **77**, 3865-3868.
23. J. Heyd and G. E. Scuseria, *J. Chem. Phys.*, 2004, **121**, 1187-1192.
24. J. Heyd, G. E. Scuseria and M. Ernzerhof, *J. Chem. Phys.*, 2006, **124**, 219906.
25. S. Grimme, *J. Comput. Chem.*, 2006, **27**, 1787-1799.
26. H. J. Monkhorst and J. D. Pack, *Phys. Rev. B*, 1976, **13**, 5188-5192.
27. S. Nosé, *J. Chem. Phys.*, 1984, **81**, 511-519.
28. A. Togo and I. Tanaka, *Scripta Mater.*, 2015, **108**, 1-5.
29. P. Giannozzi, S. Baroni, N. Bonini, M. Calandra, R. Car, C. Cavazzoni, D. Ceresoli, G. L.

Chiarotti, M. Cococcioni, I. Dabo, A. Dal Corso, S. de Gironcoli, S. Fabris, G. Fratesi, R. Gebauer, U. Gerstmann, C. Gougoussis, A. Kokalj, M. Lazzeri, L. Martin-Samos, N. Marzari, F. Mauri, R. Mazzarello, S. Paolini, A. Pasquarello, L. Paulatto, C. Sbraccia, S. Scandolo, G. Sclauzero, A. P. Seitsonen, A. Smogunov, P. Umari and R. M. Wentzcovitch, *J. Phys. Condens. Matter*, 2009, **21**, 395502.

30. Q. Wu, S. Zhang, H.-F. Song, M. Troyer and A. A. Soluyanov, *Comput. Phys. Commun.*, 2018, **224**, 405-416.
31. G. Henkelman and H. Jónsson, *J. Chem. Phys.*, 2000, **113**, 9978-9985.
32. G. Henkelman, B. P. Uberuaga and H. Jónsson, *J. Chem. Phys.*, 2000, **113**, 9901-9904.
33. W. Tang, E. Sanville and G. Henkelman, *J. Phys. Condens. Matter*, 2009, **21**, 084204.
34. A. van de Walle and G. Ceder, *J. Phase. Equilib.*, 2002, **23**, 348.
35. X. L. Sheng, Q. B. Yan, F. Ye, Q. R. Zheng and G. Su, *Phys. Rev. Lett.*, 2011, **106**, 155703.
36. F. Mouhat and F.-X. Coudert, *Phys. Rev. B*, 2014, **90**, 224104.
37. A. A. Burkov, M. D. Hook and L. Balents, *Phys. Rev. B*, 2011, **84**, 235126.
38. M. Mortazavi, C. Wang, J. Deng, V. B. Shenoy and N. V. Medhekar, *J. Power Sources*, 2014, **268**, 279-286.
39. U. Arrieta, N. A. Katcho, O. Arcelus and J. Carrasco, *Sci. Rep.*, 2017, **7**, 5350.
40. Y. Qie, J. Liu, X. Li, S. Wang, Q. Sun and P. Jena, *Physical Review Materials*, 2018, **2**.
41. S. Komaba, W. Murata, T. Ishikawa, N. Yabuuchi, T. Ozeki, T. Nakayama, A. Ogata, K. Gotoh and K. Fujiwara, *Adv. Funct. Mater.*, 2011, **21**, 3859-3867.
42. K. Nishidate and M. Hasegawa, *Phys. Rev. B*, 2005, **71**, 245418.
43. J. Liu, X. Li, Q. Wang, Y. Kawazoe and P. Jena, *J. Mater. Chem. A*, 2018, **6**, 13816-13824.
44. K. P. S. S. Hembram, H. Jung, B. C. Yeo, S. J. Pai, S. Kim, K.-R. Lee and S. S. Han, *J. Phys. Chem. C*, 2015, **119**, 15041-15046.
45. J. Zhu and U. Schwingenschlögl, *2D Materials*, 2016, **3**, 035012.
46. C. Ling and F. Mizuno, *Phys. Chem. Chem. Phys.*, 2014, **16**, 10419-10424.
47. T. Yu, Z. Zhao, L. Liu, S. Zhang, H. Xu and G. Yang, *J. Am. Chem. Soc.*, 2018, **140**, 5962-5968.
48. Y. Sun, L. Zhao, H. Pan, X. Lu, L. Gu, Y.-S. Hu, H. Li, M. Armand, Y. Ikuhara, L. Chen and X. Huang, *Nat. Commun.*, 2013, **4**, 1870.
49. A. Ponrouch, A. R. Goñi and M. R. Palacín, *Electrochem. Commun.*, 2013, **27**, 85-88.
50. C.-Y. Chou, M. Lee and G. S. Hwang, *J. Phys. Chem. C*, 2015, **119**, 14843-14850.
51. J. Zhang, R. Wang, X. Zhu, A. Pan, C. Han, X. Li, Z. Dan, C. Ma, W. Wang, H. Su and C. Niu, *Nat. Commun.*, 2017, **8**, 683.